Quasi-intrinsic colossal permittivity in Nb and In co-doped rutile TiO2 nanoceramics synthesized through a oxalate chemical-solution route combined with spark plasma sintering

Hyuksu Han, Pascal Dufour, Sungwook Mhin, Jeong Ho Ryu, Christophe Tenailleau, Sophie Guillemet-Fritsch

DOI: 10.1039/c5cp02653a

Quasi-intrinsic colossal permittivity in Nb and In co-doped rutile TiO_2 nanoceramics synthesized through a oxalate chemical-solution route combined with spark plasma sintering

HyukSu Han,[a] Pascal Dufour,[a] Sungwook Mhin,[b] Jeong Ho Ryu,[c] Christophe Tenailleau[a] and Sophie Guillemet Fritsch*[a]

Nb and In co-doped rutile TiO_2 nanoceramics (n-NITO) were successfully synthesized through a chemical-solution route combined with a low temperature spark plasma sintering (SPS) technique. The particle morphology and the microstructure of n-NITO compounds were nanometric in size. Various techniques such as X-ray diffraction (XRD), X-ray photoelectron spectroscopy (XPS), thermogravimetric (TG)/differential thermal analysis (DTA), Fourier transform infrared (FTIR), and Raman spectroscopy were used for the structural and compositional characterization of the synthesized compound. The results indicated that the as-synthesized n-NITO oxalate as well as sintered ceramic have a co-doped single phase of titanyl oxalate and rutile TiO_2, respectively. Broadband impedance spectroscopy revealed that novel colossal permittivity (CP) was achieved in n-NITO ceramics exhibiting excellent temperature-frequency stable CP (up to 10^4) as well as low dielectric loss ($\sim$5%). Most importantly, detailed impedance data analyses of n-NITO compared to microcrystalline NITO (μ-NITO) demonstrated that the origin of CP in NITO bulk nanoceramics might be related with the pinned electrons in defect clusters and not to extrinsic interfacial effects.

Introduction

Compounds exhibiting colossal permittivity (CP, $\varepsilon' > 10^3$) have been intensively studied in recent years in the search for new high performance dielectric materials in the fields of high energy density storage and microelectronic applications.[1–9] Firstly, ferroelectric perovskite or perovskite-like oxides, such as fast-fired $BaTiO_3$ (BT)[10–12] and $CaCu_3Ti_4O_{12}$ (CCTO),[13] have attracted great attention due to their high dielectric constants up to 10^5 with relatively low dielectric loss ($\tan\delta < 0.1$). However, it was revealed that CPs in these materials mainly originated from extrinsic effects, including internal barrier layer capacitance (IBLC), barrier layer capacitance (BLC), and ferroelectric effects, all of which consequently result in strong temperature-frequency dependence of dielectric properties or relatively high dielectric loss and thus impede their potential use in practical applications.[2,4,8,10–13] Therefore, the search for a new high performance CP material has been shifted to non-ferroelectric transition metal oxides such as Li and Ti co-doped NiO[9] and $La_{2-x}Sr_xNiO_4$[5]. It was demonstrated that non-ferroelectric metal oxides exhibit improved temperature-frequency stable dielectric properties with high permittivity values up to 10^5. However, their dielectric losses are also relatively high ($\tan\delta > 0.1$), becoming a roadblock for these materials to be used in the actual applications.

Recently, Hu *et al.* achieved a huge breakthrough in this area by employing highly localized electron-pinned defect dipoles.[14] They introduced co-dopants (Nb^{5+} electron-donors, In^{3+} electron-acceptors) into rutile TiO_2 (NITO), which give rise to the electrons created by both the electron and donors, and the reduction of Ti^{4+} ions is affected by the electron-acceptors in the local lattice defect clusters. Thus, the extraordinary quasi-intrinsic CP ($>10^4$) with low dielectric loss (<0.1) over a wide range of frequency (40 Hz–1 MHz) and temperature (80–450 K) is attributed to the highly localized defect dipoles in this material.

In addition, Gai *et al.* successfully fabricated amorphous NITO films onto Pt substrate using a pulsed laser deposition technique. The fabricated films exhibited CP up to 10^4 with low dielectric loss and good frequency stability (up to 10 MHz).[15]

[a] CNRS, Institut Carnot CIRIMAT, UMR CNRS UPS INP 5085, Université Paul Sabatier, 118 route de Narbonne, 31062 Toulouse Cedex 9, France. E mail: guillem@chimie.ups tlse.fr; Fax: +33 05 61 55 61 63; Tel: +33 05 61 55 62 83

[b] Korea Institute of Industrial Technology, Gaetbeol ro 156, Yeonsu gu, Incheon, 406 840, Republic of Korea

[c] Department of Materials Science and Engineering, Korea National University of Transportation, Chungju 380 702, Republic of Korea

Their work is a clear evidence, supporting the results of Hu *et al.* due to the fact that the NITO amorphous films do not have any grain boundaries, excluding grain boundary effects, and therefore the observed CP could be ascribed to the electron pinning effect in the short range atomic level. On the contrary, however, it has been recently argued that the origin of CP in microcrystalline NITO ceramics (μ-NITO) is related with the extrinsic IBLC effect rather than quasi-intrinsic highly localized defect dipoles.[16] Li *et al.* reported that NITO ceramics present inhomogeneous electrical properties within the grain and grain boundary, leading to IBLC effects and thus CP in the sintered ceramic.

Therefore, there is still ongoing debate on the origin of novel CP performance for NITO ceramics. In order to clarify this, it is essential to investigate the dielectric properties of NITO ceramics without any grain boundary effects. While this kind of investigation was performed on the NITO amorphous films,[15] it is still missing for well sintered NITO crystalline compacts. Furthermore, one can study more details about the dielectric phenomena in the NITO compound when it has a crystalline structure rather than an amorphous structure.

It is well known that for TiO_2 ceramics, electrical properties are significantly dependent on microstructure. Nanocrystalline TiO_2 show electrical homogeneity within grain and grain boundary as the material gets closer to the mesoscopic regime.[17,18] As such, dielectric phenomena of nano-crystalline NITO (n-NITO) ceramics should not be related with extrinsic grain boundary effects.

However, there is no facile and simple synthesis method for n-NITO compounds reported in the open literature to date. Thus, in this study, we report a new chemical solution route for the synthesis of n-NITO ceramics using a spark plasma sintering (SPS) technique. A detailed analysis of the electrical properties of n-NITO ceramics is performed and presented with corresponding analytical models that elucidate the origin of novel CP performance of NITO compounds.

Experimental procedure

Initially, n-NITO powders were synthesized through the oxalate precipitation method. Raw powders of commercially available $InCl_3$ (Sigma-aldrich, 98%), $NbCl_5$ (Sigma-aldrich, 99%), and lab-made $TiOCl_2$ solution (15 wt% of Ti) were used for the synthesis. $NbCl_5$ and $TiOCl_2$ were weighed following the stoichiometric composition of $(Nb_{0.5}\ In_{0.5})_{0.01}Ti_{0.99}O_2$. An additional amount of $InCl_3$ was necessary to maintain the stoichiometric composition possibly due to the higher incorporation energy of In^{3+} into the TiO_2 lattice that arises from the larger ionic radius difference between In^{3+} (r = 80 pm) and Ti^{4+} (r = 60.5 pm) ions compared to Nb^{5+} (r = 64 pm). $NbCl_5$ was dissolved in 100 mL ethanol with sonication for 30 min at room temperature. A small amount of undissolved residue (niobium oxychloride ($NbOCl_3$)), which was formed when $NbCl_5$ was exposed to air, was observed in the solution. Thus, the solution was filtered more than 2 times until the solution became transparent and then stabilized by mild stirring for 12 h at room temperature. The indium precursor solution was prepared by dissolving $InCl_3$ into 100 ml water and vigorously stirring for 20 min until the precursor is perfectly dissolved. The stabilized Nb solution was firstly mixed with $TiOCl_2$ solution (pH 1), which was dissolved in 60 mL water, and then the indium solution was subsequently mixed into the solution. The final precursor solution, which is transparent without any precipitate, was stirred again for about 10 min. Coprecipitation was performed by the addition of the final precursors into a solution of oxalic acid previously dissolved in 900 mL of ethanol. The solution was kept stirring for 5.5 h to obtain homogenously precipitated oxalates. It should be noted that oxalic acid was in 10% excess over the stoichiometric amount and that a volume ratio of 0.16 for water–ethanol was maintained for the synthesis. The precipitated oxalate was centrifuged and dried overnight at 120 °C in an oven. The dried oxalate was calcined at 1000 °C for 1 h in static air with a heating rate of 200 °C h^{-1} and finally transformed into oxide.

The calcined oxide powders were sintered using a Dr Sinter 2080 SPS system (Sumimoto Coal. Mining Co., Tokyo, Japan). 0.32 g of n-NITO powder without binder was placed in a 8 mm graphite die and then sintered at 750 °C under an applied electrical current up to 350 A combined with a mechanical pressure of 100 MPa. The powder was heated up to 750 °C using a heating rate of 100 °C min^{-1} and held at that temperature for 20 min before being finally cooled to room temperature over approximately 15 min. During SPS sintering, the inside chamber was maintained with a vacuum atmosphere ($\sim$5 Pa) *via* a dynamic vacuum controller. After sintering, a thin carbon layer was observed at the surface of the as-sintered pellets due to graphite contamination from the die. However, this layer was easily removed by polishing the surface. In order to reoxidize the as-sintered ceramics, the post-annealing process took place between 600 °C and 1100 °C for 12 h under static air. For comparison purposes, undoped TiO_2 powder and ceramic samples were also prepared through a procedure identical to the one for n-NITO samples. The density of the as-sintered and annealed samples was measured using the Archimedes method.

The particle size and morphology of the starting powders and the microstructure of the sintered ceramics were investigated using a field-emission gun scanning electron microscope (FEG-SEM, JEOL JSM 6700F). The crystal structure and phase purity were also characterized at room temperature *via* X-ray diffraction (XRD) measurements using a Bruker D4 powder diffractometer (CuK_α = 0.154056 nm and CuK_β = 0.154044 nm, operating voltage 40 kV and current 40 mA). In addition, *in situ* XRD measurements at different temperatures were performed using a Bruker D8 Advance diffractometer equipped with a furnace (Anton Pear, HTK 1200N). Raman spectroscopy was performed using a dispersive laser spectrophotometer (NRS-3100, JASCO) at room temperature with an excitation wavelength of 633 nm. The valence states of the elements in NITO compounds were analyzed by X-ray photoelectron spectroscopy (XPS, K-Alpha Thermoscientific). Thermogravimetric (TG) and differential thermal analysis (DTA) using a TGA/DTA 92 instrument from Setaram were performed under air using a heating rate of 6 °C min^{-1} up to 1000 °C. Fourier transform infrared (FTIR)

spectra were also obtained at room temperature using a Thermo Nicolet 6700 FTIR spectrometer through the KBr disk technique.

For electrical property characterization, the ceramic pellets were coated with gold (Au) electrodes using a sputter coater (Cressington 108A) for 1 min with 40 mA. The electrode samples were placed in a closed cycle workstation and broad-band impedance spectroscopy was performed as a function of frequency (40 Hz–4 MHz) at the different temperatures (250–450 K) using a precision impedance analyzer (PIA, Agilent 4294 A) combined with a temperature chamber and controller from Votsch Industrietechnik GmbH.

Results and discussion

Single phase purity of as-synthesized NITO oxalate

Fig. 1(a) shows FTIR spectra for as-synthesized TiO_2 and NITO oxalates. The FTIR spectrum of the as-synthesized NITO oxalate is almost identical with that of the as-synthesized TiO_2 oxalate; however, it is quite different from those of the individual niobium and indium oxalates.[19,20] The broad band around 3400 cm^{-1} could be attributed to the symmetric and asymmetric vibration of the O–H group, and the sharp peak at ~1676 cm^{-1} is assigned to the C O stretching vibration. The other bands at 1438, 1346, and 1303 cm^{-1} arise from O–C O asymmetric and symmetric stretch vibrations as well as the C–O stretching vibration. The bands between 900 and 650 cm^{-1} could be assigned to C–C and Ti–O vibrations. Therefore, the FTIR spectrum of as-synthesized NITO oxalate showed all the characteristic bands of titanium oxalate and hydroxyl without additional characteristic peaks from individual oxalates, indicating the formation of single phase hydroxyl titanium oxalate.[21–24]

To further demonstrate single phase purity of as-synthesized NITO oxalate, thermal analyses (TGA/DTA) were carried out on both as-synthesized TiO_2 (Fig. 1(b)) and NITO (Fig. 1(c)) oxalates. It can be clearly seen that TGA/DTA curves for NITO oxalate are quite similar to those of TiO_2 oxalate, while it is very different from those of individual oxalates.[20,25] In fact, the abrupt weight losses below 100 °C, which is observed for both niobium and indium oxalates,[20,25] are absent for both NITO and TiO_2 oxalates, suggesting that the as-synthesized NITO oxalate is not a mixture of individual oxalates but rather a single-phase titanyl oxalate. The initial weight loss of NITO oxalate (~11%) is observed at the temperature range 35–220 °C, which might be due to the liberation of surface-adsorbed and hydrated water, accompanied by an endothermic peak in the DTA curve. At the temperature range 200–600 °C, the substantial weight loss (~36%) with exothermic peaks in the DTA curve is attributed to the decomposition of titanyl oxalate to titanium oxide. In addition, the observed exothermic peak in the DTA curve at ~450 °C might be related with the transformation of TiO into TiO_2 during the decomposition of oxalate.[26] We propose three decomposition steps (labeled as eqn (1)–(3) in Fig. 1(c)), which can be described by,

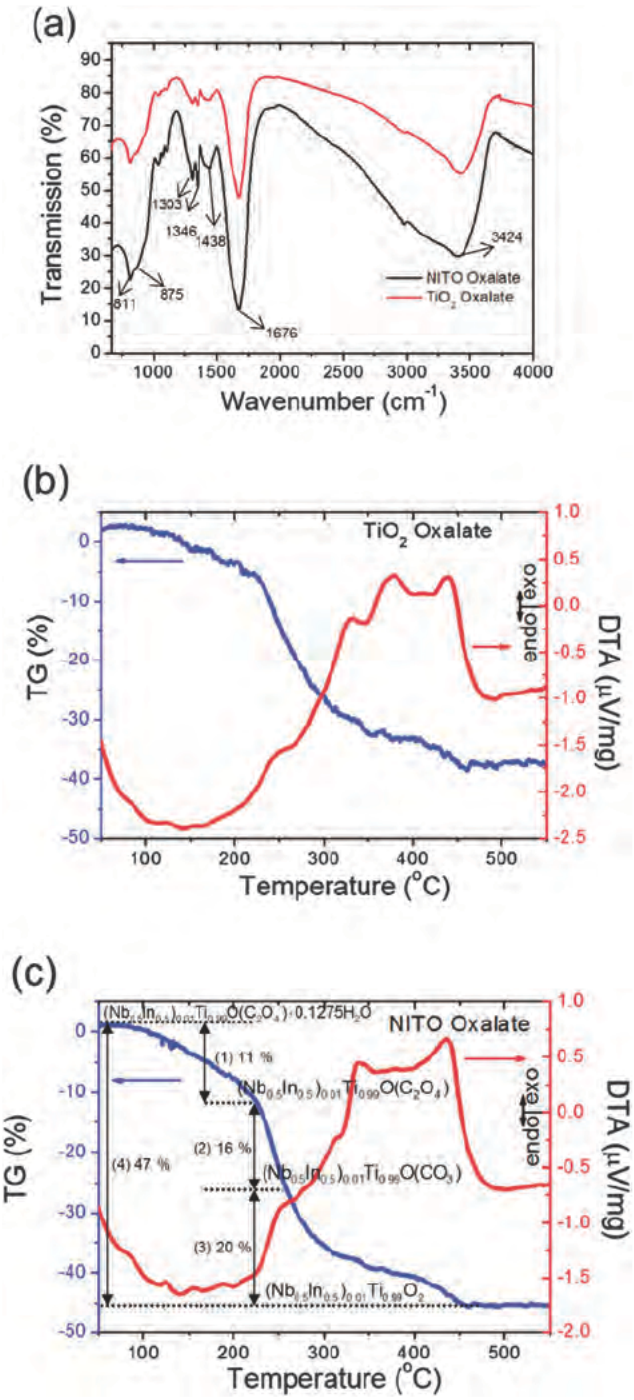

Fig. 1 (a) FTIR spectra of as synthesized TiO_2 and NITO oxalates measured by the KBr disk method. Simultaneous TG/DTA data measured at a heating rate of 6 °C min^{-1} under air for (b) TiO_2 and (c) NITO oxalates showing three decomposition steps.

$$(Nb_{0.5}In_{0.5})Ti_{0.99}O(C_2O_4)\cdot 0.1275H_2O \rightarrow (Nb_{0.5}In_{0.5})Ti_{0.99}O(C_2O_4) + 0.1275H_2O\uparrow \quad (1)$$

$$(Nb_{0.5}In_{0.5})Ti_{0.99}O(C_2O_4) \rightarrow (Nb_{0.5}In_{0.5})Ti_{0.99}O(CO_3) + CO\uparrow \quad (2)$$

$$(Nb_{0.5}In_{0.5})Ti_{0.99}O(CO_3) \rightarrow (Nb_{0.5}In_{0.5})Ti_{0.99}O_2 + CO_2\uparrow \quad (3)$$

The total weight loss of ~47%, which was measured by TG, is in good agreement with theoretically calculated weight loss of ~48% by eqn (4).

$$(Nb_{0.5}In_{0.5})Ti_{0.99}O(C_2O_4)\cdot 0.1275H_2O \rightarrow (Nb_{0.5}In_{0.5})Ti_{0.99}O_2 + CO + CO_2 + 0.1275H_2O \quad (4)$$

Moreover, we measured *in situ* XRD data for each oxalate at different temperatures (25–500 °C) and the results are presented in Fig. 2. It is clear that NITO oxalate was transformed into pure anatase TiO_2 crystal structure (PDF no. 00-021-1272) without forming any secondary phases. Furthermore, no XRD peaks from either individual oxalates (Nb oxalate,[20] In oxalate[27]) or oxides (Nb_2O_5: PDF no. 00-018-0911, In_2O_3: PDF no. 00-006-0416) were observed during the transformation of NITO oxalate into the oxide at increased temperatures. All these results confirm that the as-synthesized NITO oxalate has one single phase of Nb and In co-doped hydroxyl titanium oxalate and it is not a mixture of the oxalates of individual metal ions.

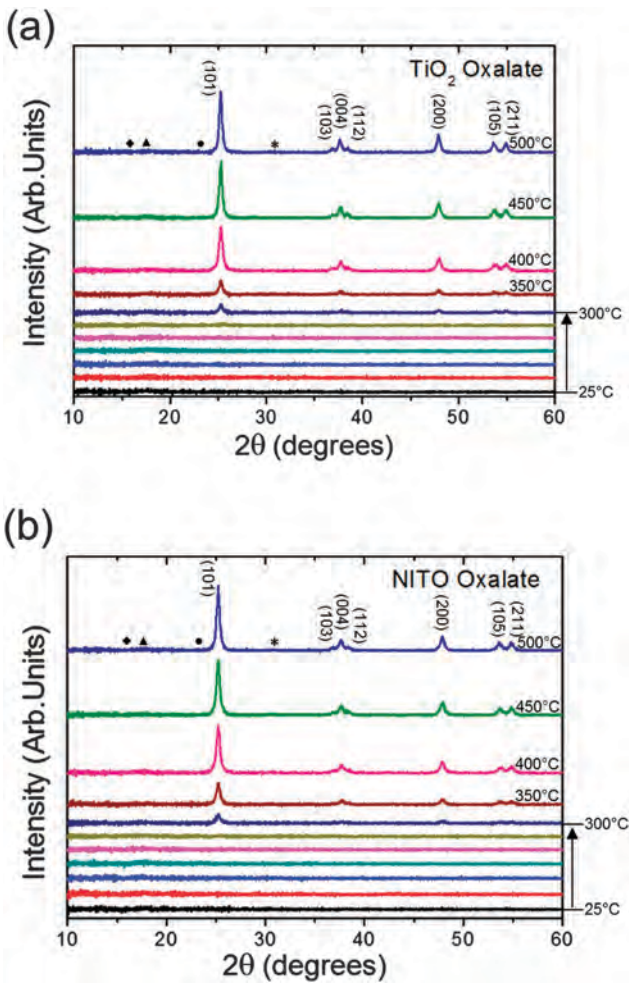

Fig. 2 XRD patterns of as synthesized (a) TiO_2 and (b) NITO oxalates measured at different temperatures from room temperature to 500 °C. Brackets indicate the theoretical XRD pattern of rutile TiO_2 (PDF no. 00 021 1272). The strongest peaks of oxalates of individual metal ions (◆ In oxalate,[27] ▲ Nb oxalate[20]) as well as oxides (● Nb_2O_5 [PDF no. 00 018 0911], *In_2O_3 [PDF no. 00 006 0416]), which are not present in the XRD patterns of NITO and TiO_2 oxalates for the temperature range, are also marked in the figure.

Structural characterization: microstructure and crystal structure

Fig. 3 represents the SEM images of the synthesized n-NITO starting powder and of the fractured surfaces for the sintered ceramics annealed at different conditions. It is clear that n-NITO powder synthesized through the chemical oxalate route has nanometric particle size with a homogenous round shape. The particle shape and size was greatly influenced by the titration rate of the ethanol solution of oxalic acid and the calcination temperature. In other words, higher reaction temperature and slower titration rate lead to a greater particle size and inhomogeneous particle morphology. The particle sizes of as-synthesized NITO oxalate and calcined n-NITO powder are determined to be 131 ± 23 nm and 201 ± 54 nm, respectively, using the Image J software. In addition, the average grain sizes of 241 ± 14 nm, 382 ± 14 nm, 580 ± 209 nm, and 1.28 ± 0.19 μm are estimated for the sintered n-NITO ceramic annealed at 600 °C, 800 °C, 900 °C, and 1100 °C, respectively, using the ASTM E112 standard method. It should be noted that for grain size measurement, although the mean lineal intercept method can only be applied for planar grains according to the ASTM E112 standard, herein, this method is used on the SEM image from the fractured surface due to the fact that the SPS sintered n-NITO samples were too brittle to observe nice planar microstructures. The samples annealed at 600 °C and 800 °C show homogeneous microstructures with nanocrystalline grains, while inhomogeneous grain growth was observed for NITO ceramics annealed at above 900 °C, and the sample annealed at 1100 °C shows microcrystalline microstructure with a grain size of 1.28 ± 0.19 μm. The density of n-NITO ceramic is determined to be ~92% for the as-sintered samples and a slight increase of density upon annealing is observed. This may indicate that a reoxidation process and elimination of some oxygen vacancies, which were created during the SPS process due to the reducing atmosphere (*i.e.*, vacuum) and fast heating rate,[28] occurred during post-annealing process.

Fig. 4(a) shows the measured XRD data for both the starting n-NITO powder and as-sintered n-NITO ceramic. The XRD patterns are typical of tetragonal rutile crystal structure (JCPDS 01-070-7347), and any secondary phase and polymorphs, such as anatase and brookite phases, are not observed for both the samples. In addition, slight peak shifts were observed in the XRD patterns of n-NITO compounds compared to those of undoped TiO_2, indicating that introduced dopants are successfully doped into the lattice without forming secondary phases. To further verify the crystal structure of as-synthesized NITO ceramic, Rietveld refinement was performed on the powder XRD data using the software Fullproof and the resulting fit reveals that the NITO sintered ceramic (Fig. 4(b)) crystallized in a pure rutile structure (space group, $P4_2/mnm$). NITO ceramic has larger lattice parameters and thus correspondingly larger unit cell volume, compared to pure TiO_2,[29] possibly due to the dopants incorporated into the lattice (Table 1).

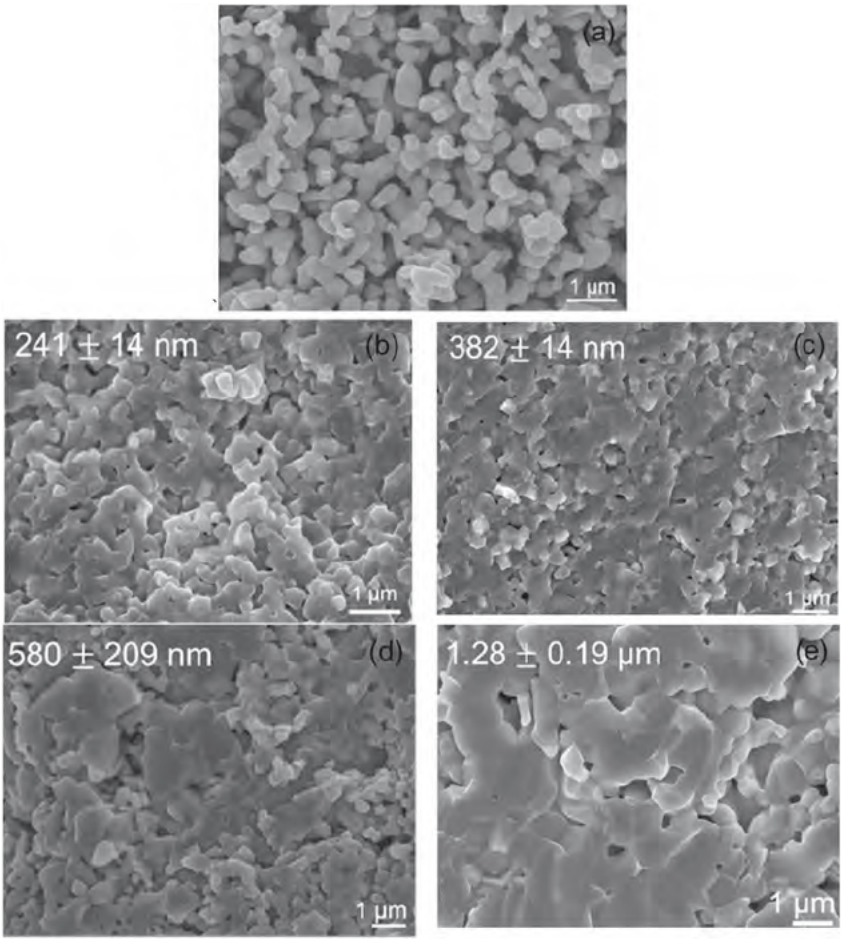

Fig. 3 SEM images of the synthesized NITO (a) starting powder and sintered ceramics which are annealed at (b) 600 °C, (c) 800 °C, (d) 900 °C, and (e) 1100 °C for 12 h. The NITO powder synthesized through a chemical solution route has nanometric particle size with round shape morphology. The sintered ceramic annealed at 600 °C has nanocrystalline microstructure while microcrystalline microstructure was observed when it annealed at 1100 °C for 12 h. Grain size of the sintered ceramics increases as annealing temperature increase.

Fig. 4(c) shows measured Raman spectra for NITO and pure TiO_2 samples. Four Raman active fundamental modes exist in rutile TiO_2, which can be assigned to B_{1g} (143 cm^{-1}), E_g (447 cm^{-1}), A_{1g} (612 cm^{-1}), and B_{2g} (826 cm^{-1}). B_{1g} and A_{1g} modes are related with O–Ti–O bond bending and Ti–O stretch modes, while the Eg mode is due to out of phase oxygen atom liberation along the *c*-axis.[30] Thus, the Raman peaks observed at 140.1 cm^{-1}, 442.8 cm^{-1}, and 609.8 cm^{-1} can be assigned to B1g, Eg, and A1g modes in rutile TiO_2, respectively, indicating that NITO compounds have the rutile phase. Note that the peak around 250 cm^{-1} is associated with the second-order Raman scattering in rutile structure.[31] In addition, NITO samples show broadened Raman peaks with lower intensities and less symmetric shapes when compared to those of pure TiO_2 samples, which might be attributed to internal stress or strain induced by the dopants.

Compositional characterization: chemical composition and valence state analysis

XRF data (not shown here) confirm that the chemical composition of the synthesized powder is well comparable with the target composition of $(Nb_{0.5}\ In_{0.5})_{0.01}Ti_{0.99}O_2$. In addition, there was little concentration variation for dopants (*i.e.*, Nb = 0.05 mol% and In = 0.05 mol%) among the oxalate, the calcined powder, and the sintered ceramics (before and after annealing), indicating that dopants are initially introduced into the lattice during the chemical coprecipitation procedure and are not volatilized while the subsequent heat treatments were performed.

In order to further provide direct evidence for doping and to determine the valence states of the elements in NITO, XPS analysis was performed on the surface of the n-NITO sample (annealed at 600 °C) and the results are presented in Fig. 5. In Fig. 5(a), the Ti 2p doublet is clearly shown at binding energies of 458.7 eV and 464.6 eV for $2p_{1/2}$ and $2p_{3/2}$, corresponding to that of pure rutile TiO_2. The spin–orbit splitting of ~5.9 eV is also consistent with that of rutile TiO_2 (5.7 eV).[32] Furthermore, a noticeable Ti^{3+} $2p_{3/2}$ signal is observed at 457.3 eV with spin–orbit splitting of ~3.9 eV. Given the comparison of colors for NITO (blue) and pure TiO_2 (milky white) annealed samples, the partial reduction of Ti^{4+} to Ti^{3+} in NITO can be attributed to the introduction of Nb^{5+} rather than the reduction atmosphere during the SPS technique,

$$Nb_2O_5 + 2TiO_2 \xrightarrow{4TiO_2} 2Nb_{Ti}^{\bullet} + 2Ti_{Ti}^{'} + 8O_O + 1/2O_2 \uparrow \quad (5)$$

$$Ti^{4+} + e \rightarrow Ti^{3+} \quad (6)$$

The O 1s profile for NITO (Fig. 5(b)) shows a main peak at 529.8 eV with a low energy tail at ~528.2 eV, which corresponds

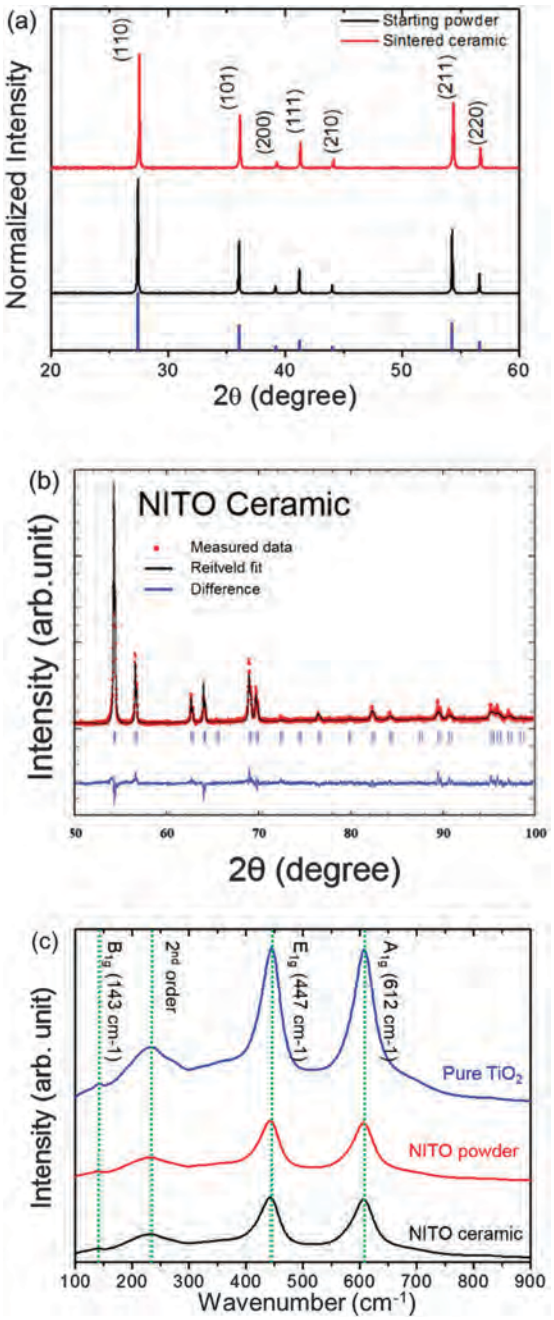

Fig. 4 (a) Measured powder XRD data for starting NITO powder and sintered NITO ceramic. (b) Rietveld refinement results for the sintered ceramic. The sintered ceramic has rutile crystal structure without any secondary phase. (c) Raman spectra for NITO powder and ceramic com pared with pure TiO2. Four characteristic peaks of TiO2 rutile phase were observed for the starting NITO powder and sintered ceramic, confirming that synthesized NITO powder and ceramic are of pure rutile phase.

Table 1 Rietveld refinement results for NITO and TiO_2 ceramics

	Space group	a (b) (Å)	c (Å)	c/a	Cell volume (Å^3)
NITO	$P4_2/mnm$	4.5961	2.9629	0.6446	62.5876
TiO_2[a]	$P4_2/mnm$	4.5937	2.9587	0.6440	62.4347

[a] Ref. 29.

to cation–oxygen bonds such as bulk Ti–O and In–Nb–O.[32] Moreover, high energy peaks around 532.2 eV and 531.2 eV are possibly related with oxygen vacancies and surface hydroxyl groups, respectively.[33] It should be noted here that Nb^{5+} dopants cannot introduce oxygen vacancies in TiO_2;[34,35] however, when the acceptor dopants are introduced in TiO_2, oxygen vacancies can be formed for charge compensation as follows,

$$In_2O_3 \xrightarrow{2TiO_2} 2In_{Ti}^{'} + V_O^{\bullet\bullet} + 3O_O \quad (7)$$

In Fig. 5(d), the In 3d profile shows that the In $3d_{3/2}$ peak with a binding energy of 444.4 eV is clearly present, indicating the existence of In^{3+} in the sample.[36] Thus, oxygen vacancies in NITO compounds can be attributed to the simultaneous doping of In^{3+} with Nb^{5+}.

The XPS results for the Nb 3d profile (Fig. 5(c)) reveals that Nb 3d electrons have binding energies of 207.3 eV and 210.1 eV for $3d_{5/2}$ and $3d_{3/2}$, respectively. The spin–orbit splitting of 2.8 eV is consistent with that of Nb^{5+} doped TiO_2.[34,37] Moreover, the doublet of Nb $3d_{5/2}$ indicates the presence of Nb^{4+}, which might be attributed to the reduction of Nb^{5+} to Nb^{4+} during the post-annealing process. In addition, the quantitative analysis of the XPS data confirms that the concentrations of In and Nb are 0.35 at% and 0.37 at%, respectively, which is in good agreement with the target concentrations.

All of the abovementioned results confirm that rutile n-NITO ceramics are successfully synthesized through the chemical solution route combined with a low-temperature SPS sintering technique. To the best of our knowledge, this is the first report of a synthesis technique for n-NITO ceramic that exhibits controlled dopant concentrations, powder morphology, crystal phase, and microstructure. A new and facile solution-chemistry approach for the synthesis of n-NITO compounds, presented in this study, is important given that it might contribute to not only revealing the ongoing debate related with the origin of extraordinary dielectric behaviors of NITO ceramics but also to the tailoring of their functional properties through nano- and micro-structure engineering.

Impedance data analysis: homogeneous electrical property in n-NITO

Fig. 6(a) shows the dielectric properties of n-NITO and TiO_2 ceramics as a function of frequency (40 Hz–1 MHz) at room temperature. It is clear that the relative permittivity of the n-NITO ceramic is significantly increased (two orders of magnitude) compared to undoped TiO_2 ceramic, and a relative permittivity up to 10^4 is maintained over the wide range of frequencies, suggesting that an excellent frequency-stable CP is achieved in the n-NITO ceramic. Furthermore, dielectric loss for the n-NITO

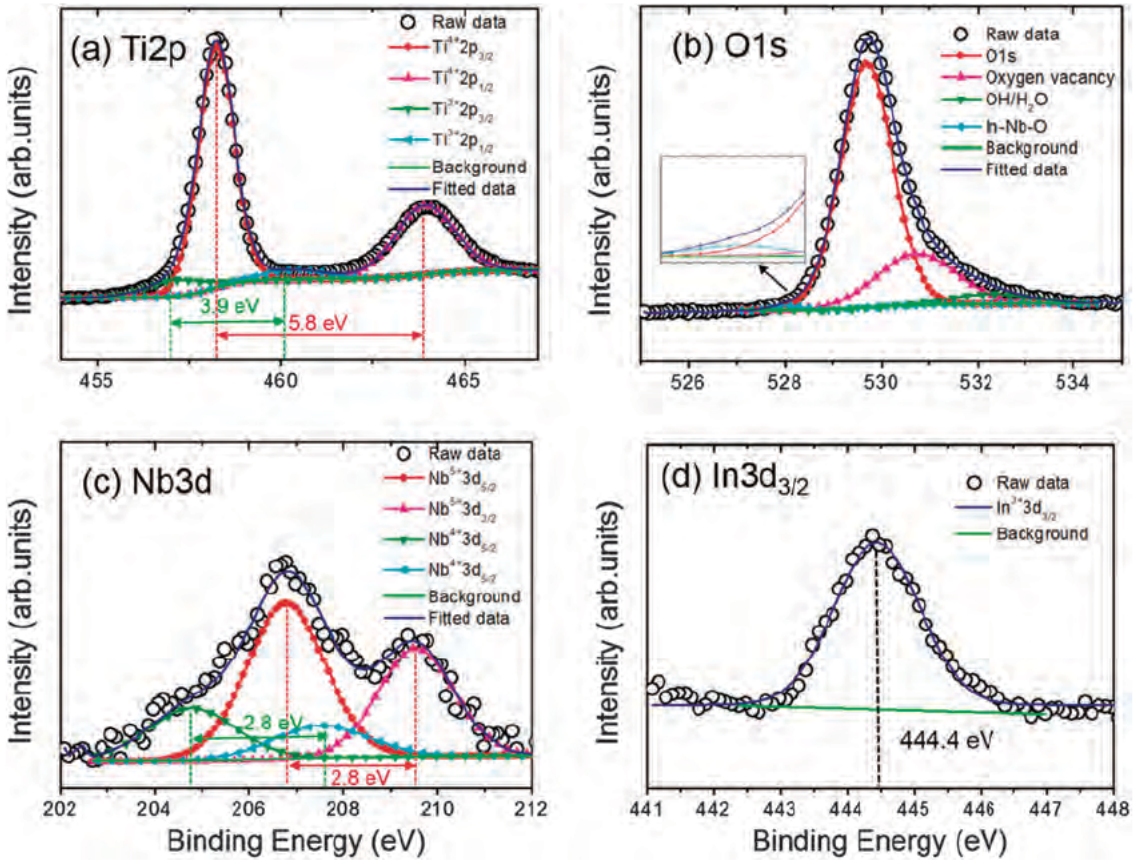

Fig. 5 Valence state characterization for NITO ceramics. Core level XPS (open circles) and corresponding fitting results (solid lines) of (a) Ti 2p, (b) O 1s, (c) Nb 3d, and (d) In $3d_{3/2}$ electrons of 1% (Nb + In) co doped TiO_2.

($\tan\delta = 0.07$ at 1 kHz) is much lower than that of the TiO_2 ($\tan\delta = 0.22$ at 1 kHz). In addition, while the dielectric loss of TiO_2 is strikingly increased (up to 0.8) as frequency decreases, $\tan\delta$ below 0.1 is maintained for the n-NITO sample over the frequency range from 1 kHz to 1 MHz. Fig. 6(b) shows the dielectric properties of the n-NITO sample as a function of temperature (250–450 K) at different frequencies. From Fig. 6(b), it can be seen that the dielectric properties of n-NITO show excellent temperature stability over the relatively wide range of temperatures at measured frequencies. It is observed that the dielectric loss of n-NITO shows better temperature dependency at higher frequencies, which might be attributed to oxygen vacancies at the grain boundary whose relaxation frequency around 1 kHz.[8,16,38] These results obviously demonstrate that a novel CP performance is achieved in n-NITO compounds by chemically introducing co-dopants (*i.e.*, In and Nb) into the TiO_2 lattice.

More importantly, it should be denoted here that for n-NITO ceramics, dielectric relaxation is not observed at the high frequency range between 10^5 Hz and 10^6 Hz (Fig. 6(a)), wherein CP materials, including microcrystalline μ-NITO ceramics,[16] generally show distinct relaxations for interfacial polarization associated with blocked space charges at grain boundaries.[10,12,39] This might imply either that n-NITO ceramics may have electrically homogeneous microstructures enabling the dismissal of a typical IBLC effect, or that dipoles related with any space charges, such as electrons, oxygen vacancies, and point defects for compensating extrinsic dopants, are highly localized at the atomic level. This will be further discussed in detail in the following sections.

Fig. 7(a) shows the impedance spectrum of the n-NITO sample (open circle) measured at different temperatures, wherein Fig. 7(b) is an enlarged view of high frequency region. Only one depressed semicircle is observed for the n-NITO ceramic, which is distinctly different from that of the μ-NITO exhibiting two different impedance arcs and each arc corresponds to bulk and blocking grain boundary responses.[16] It is reported that for nanocrystalline TiO_2 ceramics, the specific grain boundary resistivity is orders of magnitude lower than that of microcrystalline samples due to size-dependent impurity segregation. In other words, the impurity atoms, which lead to grain boundary blocking, cannot be completely saturated at grain boundaries due to the large specific grain boundary area in nanocrystalline compacts.[40,41] Therefore, the time constants for bulk and blocking grain boundaries become comparable to each other, and then bulk and grain boundary responses overlap, resulting in only one depressed semicircle in the impedance data plot.[18,41,42] This phenomena is also observed in various nanocrystalline ceramics such as CeO_2,[43] $SrTiO_3$,[44] and Yb doped $SrCeO_3$.[45]

The impedance data of n-NITO are fitted (solidus line) using equivalent circuit as presented in the inset of Fig. 7(a), and the

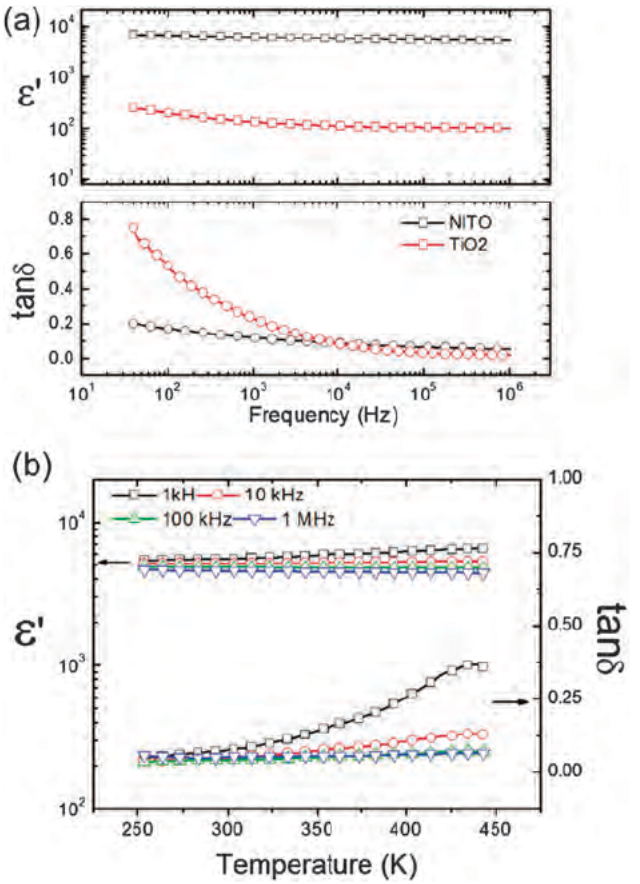

Fig. 6 (a) Dielectric properties of n NITO and undoped TiO_2 samples as a function of frequency (40 Hz 1 MHz) at room temperature. (b) Temperature dependent dielectric properties of n NITO sample at different frequencies.

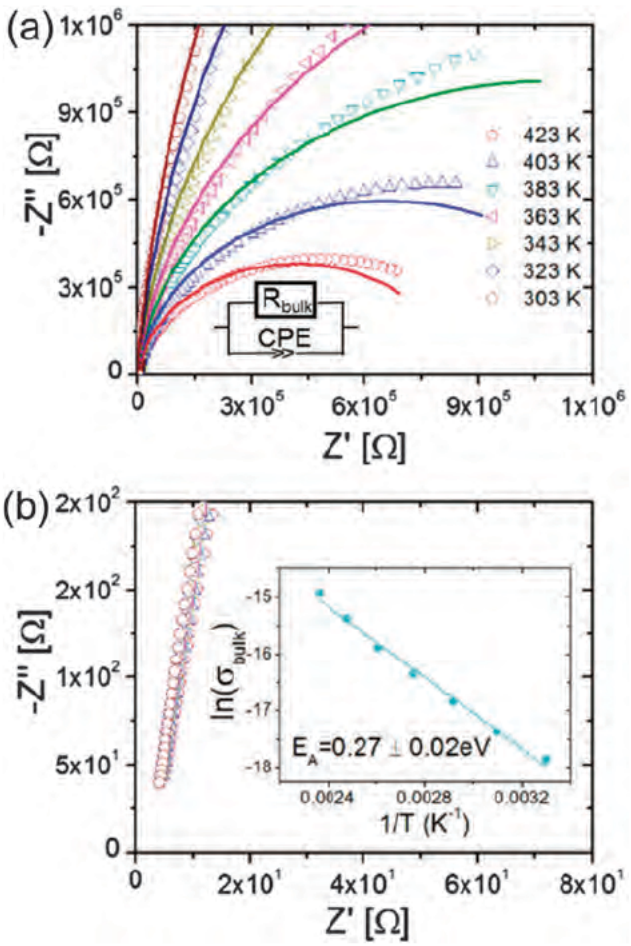

Fig. 7 (a) Complex impedance plots [$Z'(\omega)$ $Z''(\omega)$] (40 Hz 5 MHz) open dots of n NITO sample measured from 303 K to 423 K with corresponding fitting results (solid lines) using an equivalent circuit. (b) Enlarged view of the high frequency data of complex impedance plots with temperature dependent dc bulk conductivity (inset of the figure) where the solid symbols are the experimental results and the solid line is the fitting result.

fitting parameters for CPE and R values are obtained. A relative permittivity of 6604 is calculated for the bulk response of the n-NITO at room temperature by following the relationship,

$$C = R^{(1-n)/n}\, Q^{1/n} \qquad (8)$$

where C, R, Q, and n represent the true capacitance, the resistance, the pseudo-capacitance, and an additional parameter, respectively. The calculated permittivity is in good agreement with experimental results (Fig. 6(a)), indicating the measured data is representative of the bulk response. Moreover, the temperature-dependent bulk conductivity (σ_{bulk}) is calculated for the n-NITO and is plotted following the Arrhenius-type nearest neighboring hopping model, wherein $\ln\sigma$ has a linear relationship with $1/T$ (shown in the inset of Fig. 7(b)).[46] The bulk conductivity data fits well using the Arrhenius model, and an activation energy ($E_{A,\sigma bulk}$) of 0.27(2) eV is extracted. The activation energy of n-NITO for bulk conduction is found to be less than that of μ-NITO (E_a = 0.63 eV), which corresponds to the activation energy of Maxwell–Wagner polarization in rutile TiO_2.[16] The lower activation energy for n-NITO can probably be ascribed to the effect of space charge potential, which plays a much more significant role in the nanocrystalline materials as the electrical properties are dominated by the mesoscopic regime.[44,47] The impedance data of the n-NITO clearly prove that the n-NITO ceramic has homogeneous electrical properties throughout the microstructure and thus the typical IBLC effect cannot influence the dielectric properties of the n-NITO ceramic. Nevertheless, since extraordinary CP behaviors are still present in the n-NITO sample, one can conclude that CP in NITO compounds might have nothing to do with extrinsic interfacial effects.

Dielectric properties and polarization mechanisms: n-NITO *vs.* μ-NITO

To further demonstrate homogeneous electrical properties of n-NITO, dielectric properties of NITO ceramics annealed at different temperatures are presented in Fig. 8. Relative permittivity dropped one magnitude of order as annealing temperature increased from 800 °C to 900 °C, and no significant change in relative permittivity was observed upon further increase of annealing temperature. Dielectric losses also decrease as annealing temperature increases. However, it is important to note that dielectric loss at high frequency (above 10 kHz) shows

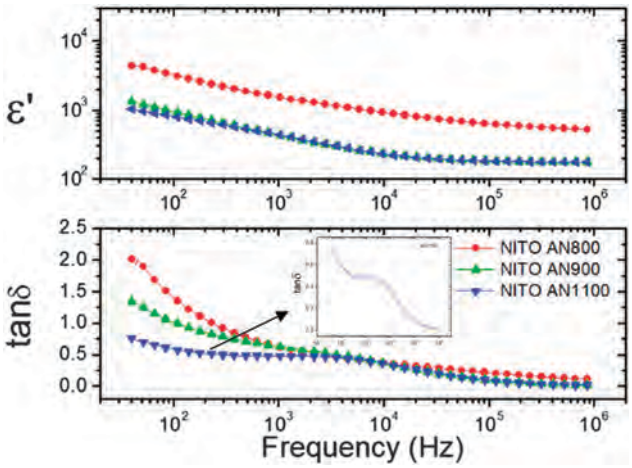

Fig. 8 Dielectric properties of NITO samples annealed at different tem peratures (800 °C, 900 °C, and 1100 °C) as a function of frequency (40 Hz 1 MHz) at room temperature. The inset shows dielectric relaxation of μ NITO at high frequency range.

little dependence on annealing temperature, while dielectric loss at low frequency (below 10 kHz) significantly decreases as annealing temperature increases. This might be due to the fact that as annealing temperature increases, charge defect species, such as impurities, dopants, and vacancies, can migrate towards grain boundaries, and thus the resistivity of grain boundary can be enhanced due to the segregation of charged species at grain boundaries, resulting in low dielectric losses at low frequencies. More importantly, dielectric relaxation was observed for the μ-NITO sample (annealed at 1100 °C) at frequency range of 1–10 kHz (the inset of Fig. 8), indicating interfacial polarization might be present in μ-NITO sample.

Fig. 9 shows dielectric properties of n-NITO and μ-NITO samples as a function of frequency (40 Hz–4 MHz) at different temperatures (303–423 K). As can be seen in Fig. 9(a), the dielectric properties of μ-NITO show much higher temperature-frequency dependence compared to the n-NITO sample (Fig. 9(b)). Furthermore, thermally activated Debye-like dielectric relaxation is clearly observed at high frequency (above 1 kHz) for μ-NITO, which can be confirmed by dielectric loss peaks at relaxation frequencies that shift to higher frequencies at higher temperatures. This type of high frequency relaxation was absent in the n-NITO sample, with loss values that show little temperature dependence at high frequencies and finally merged as frequency increased above 1 MHz.

Electrical modulus is often considered as a more effective formalism for investigating defect relaxation in polycrystalline ceramics since the effect of mobile charge carriers on relaxation can be ruled out in this formalism.[38,48] Complex modulus M^* can be written as,[49]

$$M^* = M' + M'' = 1/\varepsilon^* = 1/(\varepsilon \quad i\varepsilon'') = \varepsilon'/(\varepsilon'^2 + \varepsilon''^2) + i\varepsilon''/(\varepsilon'^2 + \varepsilon''^2) \tag{9}$$

where i, ε^*, ε', and ε'' are $\sqrt{\ }$ 1, complex permittivity, real and imaginary part of complex permittivity, and $M' = \varepsilon'/(\varepsilon'^2 + \varepsilon''^2)$ and $M'' = \varepsilon''/(\varepsilon'^2 + \varepsilon''^2)$ are the real and the imaginary part of the complex modulus, respectively.

Fig. 9(c) shows both the imaginary part of the complex modulus and impedance for μ-NITO and n-NITO samples, respectively. It is worth noting here that the impedance peak height Z_{max}'' is proportional to "R" for that particular element, while M_{max}'' is inversely proportional to "C" for the element. Thus, the impedance of the materials that are electrically inhomogeneous (*i.e.* more than one RC element) can be dominated by grain boundary resistance for the overall frequency range, suppressing the grain response at high frequency region. However, the grain response can appear in the imaginary part of the modulus plot since the modulus plots pick out the

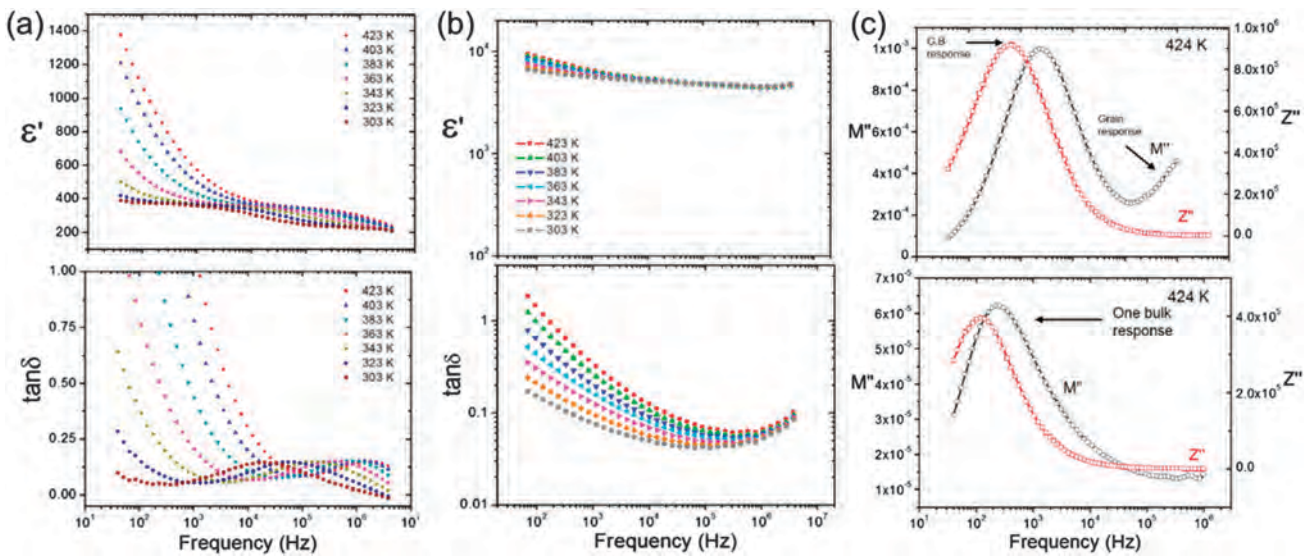

Fig. 9 Dielectric properties of (a) μ NITO and (b) n NITO samples as a function of frequency (40 Hz 4 MHz) at different temperatures (303 423 K), which demonstrates existence of dielectric relaxation at high frequency range for μ NITO sample. (c) Modulus and impedance plots for μ NITO (upper) and n NITO (below) samples measured at 424 K.

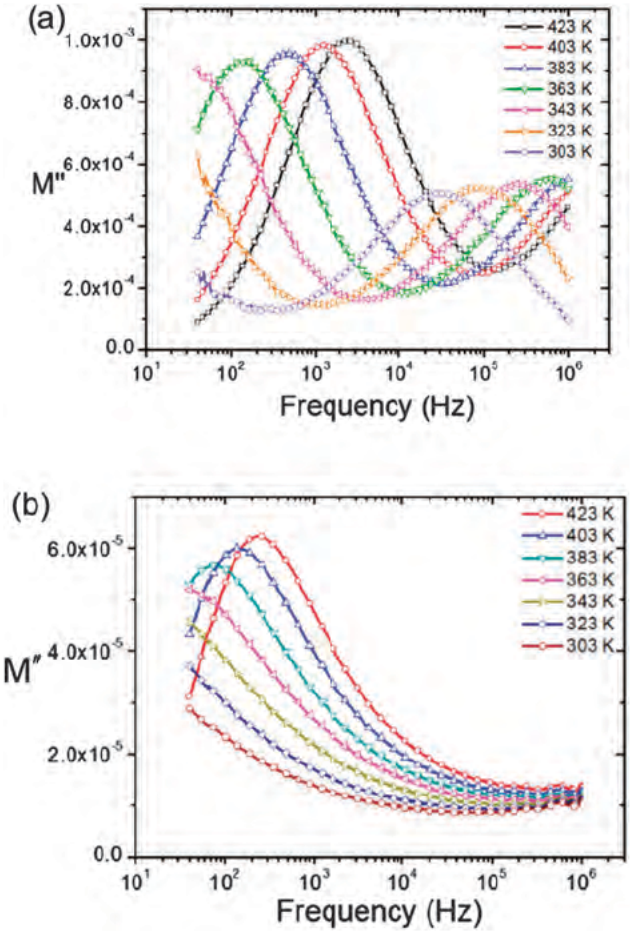

Fig. 10 The imaginary part of the modulus for (a) μ NITO and (b) n NITO samples as a function of frequency (40 Hz 1 MHz) at different tempera tures (303 423 K). Two different relaxations at low and high frequency ranges are clearly presented for the μ NITO sample while only one relaxation is observed for the n NITO sample.

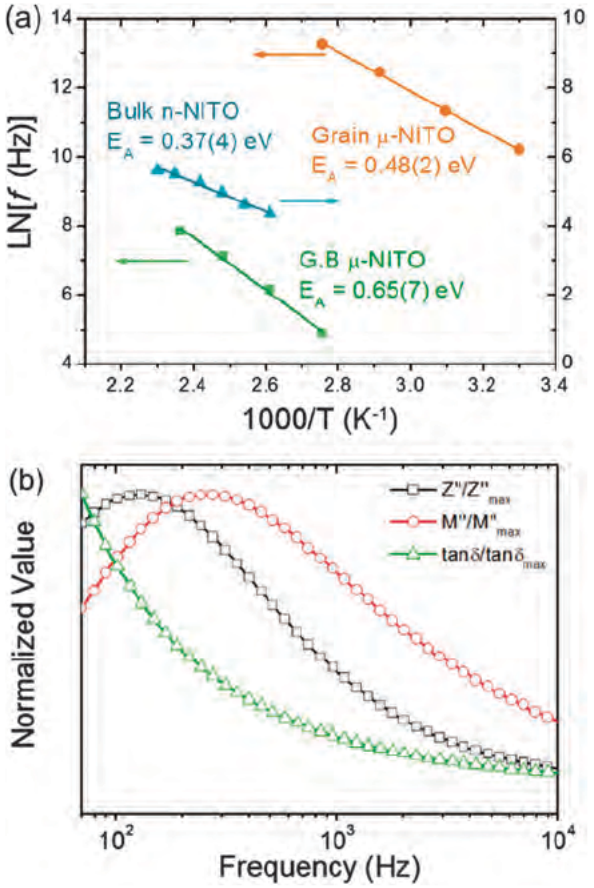

Fig. 11 (a) The relaxation frequencies as a function of temperature, wherein the solid symbols are the experimental relaxation frequencies and the solid line is the fitting result for both μ NITO and n NITO samples. (b) Frequency dependencies of normalized peaks, M'', Z'', and tanδ, of n NITO sample at 443 K.

elements with the smallest capacitance (*i.e.* grains). As a consequence, the resulting M'' and Z'' spectra may look very different for the materials, which are electrically inhomogeneous.

Sharp increases in the imaginary part of the modulus is clearly presented at high frequency region for μ-NITO (Fig. 9(c)), while a long tail-like shape is observed for n-NITO sample. Furthermore, high frequency response is not observed in the imaginary part of the impedance plots for the both the μ-NITO and n-NITO samples. These results clearly indicate that n-NITO is electrically homogeneous over the microstructure, which can be demonstrated by only one bulk response in the modulus plot, while μ-NITO has an electrically inhomogeneous microstructure, which might be composed of semiconductive grains and resistive grain boundaries.

Fig. 10 shows M'' *vs.* frequency plots at different temperatures for μ-NITO and n-NITO samples. Two different relaxations following the thermally activated Arrhenius model are clearly observed for μ-NITO at low and high frequency regions, respectively, while only one relaxation is present in M'' *vs.* frequency plots for the n-NITO sample. Activation energy for the relaxation ($E_{A,rix}$) can be calculated based on the following equation,

$$f_{max} = f_0 \left[E_{A,rix}/(\quad KT)\right] \qquad (10)$$

where f_{max}, f_0, and k are the maximum frequency of the imaginary part of the modulus at each temperature, relaxation frequency, and the Boltzmann constant, respectively. Fig. 11(a) shows experimental data with a fitted curve using the above model for both μ-NITO and n-NITO samples. From the fitting results, the values of $E_{A,rix}$ are determined to be 0.37(4) eV, 0.65(7) eV, and 0.48(2) eV for the bulk of n-NITO, the grain boundary, and the grain of μ-NITO, respectively. It is found for n-NITO that the relaxation phenomena have significantly lower activation energies compared to those of μ-NITO. More importantly, $E_{A,rix}$ of μ-NITO (0.65(7) eV, 0.48(2) eV) is comparable with $E_{A,rix}$ of oxygen vacancy at the grain boundaries in various titanium oxides and hence the dielectric relaxation in μ-NITO may be associated with the Maxwell–Wagner-type polarization at the grain boundary, which also can be confirmed by the existence of two different relaxations for the grain and the grain boundary, resulting in the IBLC effect in μ-NITO.[8,16,38]

Moreover, the homogeneous electrical properties of n-NITO are thought to be associated with the advantages of processing techniques employed here. In other words, firstly, doping of In and Nb was accomplished at room temperature through the chemical-solution process and the subsequent calcination process was also done at much lower temperature (1000 °C) and shorter time (1 h) compared to the conventionally synthesized NITO through solid-state processing (1450 °C for 10 h).[16] Therefore, the starting n-NITO powder, synthesized through chemical solution route, should have much more homogeneous dopant distribution in the starting material, which can result in electrically homogeneous microstructures of the sintered ceramic if the powder can be sintered at very low temperature. It is noted that we could transform NITO oxalate to oxide by calcination at as low as 500 °C for 1 h; however, a calcination temperature of 1000 °C was used in order to obtain 100% rutile phase. Secondly, the SPS technique enables us to use a fast heating rate of up to 600 °C min^{-1} and a lower sintering temperature (here 750 °C) thanks to Joule heating and high mechanical pressure applied during the process, respectively. Thus, the SPS technique can minimize impurity segregation at the grain boundaries of sintered ceramics, which results in lower resistivity of the grain boundary compared to that of conventionally sintered ceramics.[50,51] Hence, the chemical solution route combined with the SPS technique is an effective way of synthesizing electrically homogeneous n-NITO ceramics, while NITO ceramics synthesized through a conventional solid-state route may inevitably have an IBLC effect for dielectric properties due to electrically inhomogeneous microstructures arising from high temperature processing conditions.

Lastly, plotting a.c. data in terms of M''/M_{max}'', $\tan\delta/\tan\delta_{max}$, and Z''/Z_{max}'' simultaneously is a powerful way of determining the dynamic nature of polaronic particles whether the response being measured is due to localized relaxation or to long range conductivity. Namely, each dielectric function (*i.e.*, ε^*, M^*, and Z^*) has its own relaxation time for the same relaxation process, and thus a peak in the imaginary part of the function appears at different frequencies depending on the dielectric strength.[52,53] For a parallel RC circuit, the dielectric functions can be written as,

$$\varepsilon^* = \varepsilon_\infty(1 \quad i\omega\tau) \tag{11}$$

$$\tan\delta = 1/\omega\tau \tag{12}$$

$$Z^* = R/(1 + i\omega\tau) \tag{13}$$

$$M^* = 1/[\varepsilon_\infty(1 \quad i\omega\tau)] \tag{14}$$

where $\omega = 2\pi f$ is angular frequency, $\tau = RC$ is the relaxation time for the long range conduction, and ε_∞ is the real permittivity at infinite frequency. According to Gerhardt *et al.*, the above equations leads to the conclusion that τ_Z and τ_M should have finite values, which are exactly equal or very similar to each other, and therefore the peak positions of the two plots should be overlapped for a bulk response with long range nature.[52–54] However, for the n-NITO sample, Fig. 11(b) apparently shows that the peak positions of the M''/M_{max}'' and Z''/Z_{max}'' curves are not overlapped, suggesting the bulk response of n-NITO is due to localized relaxation rather than long range conduction. Therefore, the polarization mechanism of CP in n-NITO is due to the highly localized electrons possibly in the local defect clusters created by the combined effect of Ti reduction and extrinsic dopants.

Conclusion

In conclusion, we reported a novel chemical-solution synthesis route with low temperature sintering technique for n-NITO ceramics. The dense n-NITO ceramic sintered at significantly low sintering temperature (750 °C) using nanopowders shows homogeneous electrical properties throughout the microstructure, enabling the investigation of dielectric properties of the compound regardless of extrinsic interfacial effects. The low temperature processing techniques applied in this study may lead to homogeneous dopant distribution in the sintered ceramic and thus homogeneous electrical properties throughout the microstructure. Various analysis techniques, such as FTIR, *in situ* XRD, and TG/DTA, confirm that the chemical-solution route combined with spark plasma sintering is a promising way to directly synthesize Nb and In co-doped TiO_2 nanoceramics with controlled composition, crystal structure, and phase. Furthermore, comparison of impedance data between n-NITO and μ-NITO samples reveals that a key factor for achieving quasi-intrinsic CP in NITO compounds is to sinter the ceramic to produce electrically homogeneous microstructures that fully induce pinned electrons in the localized defect clusters and avoid the Maxwell–Wagner-type interfacial polarization effect.

Acknowledgements

The authors thank FERMAT federation for funding, I. Pasquet for FEG-SEM images, and B. Duployer for XRF measurements.

References

1 H. F. Hess, K. Deconde, T. F. Rosenbaum and G. A. Thomas, *Phys. Rev. B: Condens. Matter Mater. Phys.*, 1982, **25**, 5578–5580.
2 C. C. Homes, T. Vogt, S. M. Shapiro, S. Wakimoto and A. P. Ramirez, *Science*, 2001, **293**, 673–676.
3 N. Ikeda, H. Ohsumi, K. Ohwada, K. Ishii, T. Inami, K. Kakurai, Y. Murakami, K. Yoshii, S. Mori, Y. Horibe and H. Kito, *Nature*, 2005, **436**, 1136–1138.
4 B. G. Kim, S. M. Cho, T. Y. Kim and H. M. Jang, *Phys. Rev. Lett.*, 2001, **86**, 3404–3406.
5 S. Krohns, P. Lunkenheimer, C. Kant, A. V. Pronin, H. B. Brom, A. A. Nugroho, M. Diantoro and A. Loidl, *Appl. Phys. Lett.*, 2009, **94**, 122903.
6 S. Krohns, P. Lunkenheimer, S. Meissner, A. Reller, B. Gleich, A. Rathgeber, T. Gaugler, H. U. Buhl, D. C. Sinclair and A. Loidl, *Nat. Mater.*, 2011, **10**, 899–901.
7 M. Shu-Nan and M. Maki, *J. Phys. Soc. Jpn.*, 2011, **80**, 084706.

8 C. C. Wang and L. W. Zhang, *Appl. Phys. Lett.*, 2006, **88**, 042906.
9 J. B. Wu, C. W. Nan, Y. H. Lin and Y. Deng, *Phys. Rev. Lett.*, 2002, **89**, 217601.
10 S. Guillemet-Fritsch, Z. Valdez-Nava, C. Tenailleau, T. Lebey, B. Durand and J. Y. Chane-Ching, *Adv. Mater.*, 2008, **20**, 551–555.
11 Z. Valdez-Nava, S. Guillemet-Fritsch, C. Tenailleau, T. Lebey, B. Durand and J. Y. Chane-Ching, *J. Electroceram.*, 2009, **22**, 238–244.
12 H. Han, C. Voisin, S. Guillemet-Fritsch, P. Dufour, C. Tenailleau, C. Turner and J. C. Nino, *J. Appl. Phys.*, 2013, **113**, 024102.
13 M. A. Subramanian, D. Li, N. Duan, B. A. Reisner and A. W. Sleight, *J. Solid State Chem.*, 2000, **151**, 323–325.
14 W. B. Hu, Y. Liu, R. L. Withers, T. J. Frankcombe, L. Noren, A. Snashall, M. Kitchin, P. Smith, B. Gong, H. Chen, J. Schiemer, F. Brink and J. Wong-Leung, *Nat. Mater.*, 2013, **12**, 821–826.
15 Z. G. Gai, Z. X. Cheng, X. L. Wang, L. L. Zhao, N. Yin, R. Abah, M. Zhao, F. Hong, Z. Y. Yu and S. X. Dou, *J. Mater. Chem. C*, 2014, **2**, 6790–6795.
16 J. L. Li, F. Li, Y. Y. Zhuang, L. Jin, L. H. Wang, X. Y. Wei, Z. Xu and S. J. Zhang, *J. Appl. Phys.*, 2014, **116**, 074105.
17 K. K. Adepalli, M. Kelsch, R. Merkle and J. Maier, *Phys. Chem. Chem. Phys.*, 2014, **16**, 4942–4951.
18 P. Knauth and H. L. Tuller, *J. Appl. Phys.*, 1999, **85**, 897–902.
19 T. Kebede, B. B. V. Sailaja and M. S. P. Rao, *Oxid. Commun.*, 2014, **37**, 687–695.
20 T. T. Su, Y. C. Zhai, H. Jiang and H. Gong, *J. Therm. Anal. Calorim.*, 2009, **98**, 449–455.
21 F. H. Liu, G. J. Xu, J. H. Wu, Y. C. Cheng, J. J. Guo and P. Cui, *Smart Mater. Struct.*, 2009, **18**, 125015.
22 T. Berger, A. Rodes and R. Gomez, *Phys. Chem. Chem. Phys.*, 2010, **12**, 10503–10511.
23 J. Fang, F. Wang, K. Qian, H. Z. Bao, Z. Q. Jiang and W. X. Huang, *J. Phys. Chem. C*, 2008, **112**, 18150–18156.
24 T. Thongtem and S. Thongtem, *Ceram. Interfaces*, 2004, **30**, 1463–1470.
25 Z. X. Chen, Y. M. Zhou, L. H. Weng, H. Y. Zhang and D. Y. Zhao, *J. Solid State Chem.*, 2003, **173**, 435–441.
26 H. S. Potdar, S. B. Deshpande and S. K. Date, *Mater. Chem. Phys.*, 1999, **58**, 121–127.
27 N. Audebrand, S. Raite and D. Louer, *Solid State Sci.*, 2003, **5**, 783–794.
28 H. Han, D. Ghosh, J. L. Jones and J. C. Nino, *J. Am. Ceram. Soc.*, 2013, **96**, 485–490.
29 C. J. Howard, T. M. Sabine and F. Dickson, *Acta Crystallogr., Sect. B: Struct. Sci.*, 1991, **47**, 462–468.
30 A. Gajovic, M. Stubicar, M. Ivanda and K. Furic, *J. Mol. Struct.*, 2001, **563**, 315–320.
31 C. A. Melendres, A. Narayanasamy, V. A. Maroni and R. W. Siegel, *J. Mater. Res.*, 1989, **4**, 1246–1250.
32 B. Erdem, R. A. Hunsicker, G. W. Simmons, E. D. Sudol, V. L. Dimonie and M. S. El-Aasser, *Langmuir*, 2001, **17**, 2664–2669.
33 E. Ramos-Moore, P. Ferrari, D. E. Diaz-Droguett, D. Lederman and J. T. Evans, *J. Appl. Phys.*, 2012, **111**, 014108.
34 D. Morris, Y. Dou, J. Rebane, C. E. J. Mitchell, R. G. Egdell, D. S. L. Law, A. Vittadini and M. Casarin, *Phys. Rev. B: Condens. Matter Mater. Phys.*, 2000, **61**, 13445–13457.
35 M. Valigi, D. Cordischi, G. Minelli, P. Natale, P. Porta and C. P. Keijzers, *J. Solid State Chem.*, 1988, **77**, 255–263.
36 J. Q. Xu, Y. P. Chen, Q. Y. Pan, Q. Xiang, Z. X. Cheng and X. W. Dong, *Nanotechnology*, 2007, **18**, 115615.
37 A. Dacca, G. Gemme, L. Mattera and R. Parodi, *Appl. Surf. Sci.*, 1998, **126**, 219–230.
38 J. Y. Li, X. T. Zhao, F. Gu and S. T. Li, *Appl. Phys. Lett.*, 2012, **100**, 202905.
39 Z. Valdez-Nava, C. Tenailleau, S. Guillemet-Fritsch, N. El Horr, T. Lebey, P. Dufour, B. Durand and J. Y. Chane-Ching, *J. Phys. Chem. Solids*, 2011, **72**, 17–23.
40 P. Knauth and H. L. Tuller, *Solid State Ionics*, 2000, **136**, 1215–1224.
41 M. Aoki, Y. M. Chiang, I. Kosacki, I. J. R. Lee, H. Tuller and Y. P. Liu, *J. Am. Ceram. Soc.*, 1996, **79**, 1169–1180.
42 C. D. Terwilliger and Y. M. Chiang, *Acta Metall. Mater.*, 1995, **43**, 319–328.
43 Y. M. Chiang, E. B. Lavik, I. Kosacki, H. L. Tuller and J. Y. Ying, *Appl. Phys. Lett.*, 1996, **69**, 185–187.
44 P. Balaya, J. Jamnik, J. Fleig and J. Maier, *Appl. Phys. Lett.*, 2006, **88**, 062109.
45 I. Kosacki and H. U. Anderson, *Sens. Actuators, B*, 1998, **48**, 263–269.
46 A. K. Jonscher, *Universal Relaxation Law*, Chelsea Dielectrics, 1996.
47 J. Maier, *Chem. Mater.*, 2014, **26**, 348–360.
48 B. Roling, A. Happe, K. Funke and M. D. Ingram, *Phys. Rev. Lett.*, 1997, **78**, 2160–2163.
49 R. Tripathi, A. Kumar, C. Bharti and T. P. Sinha, *Curr. Appl. Phys.*, 2010, **10**, 676–681.
50 Z. A. Munir, U. Anselmi-Tamburini and M. Ohyanagi, *J. Mater. Sci.*, 2006, **41**, 763–777.
51 X. Chen, K. A. Khor, S. H. Chan and L. G. Yu, *Mater. Sci. Eng., A*, 2004, **374**, 64–71.
52 R. Gerhardt, *J. Phys. Chem. Solids*, 1994, **55**, 1491–1506.
53 W. Q. Cao and R. Gerhardt, *Solid State Ionics*, 1990, **42**, 213–221.
54 I. M. Hodge, M. D. Ingram and A. R. West, *J. Electroanal. Chem.*, 1976, **74**, 125–143.